PNAS RESEARCH ARTICLE | CHEMISTRY

High-Mg calcite nanoparticles within a low-Mg calcite matrix: A widespread phenomenon in biomineralization

Nuphar Bianco-Stein[a,b], Iryna Polishchuk[a,b], Arad Lang[a,b], Lotan Portal[a,b], Catherine Dejoie[c], Alexander Katsman[a,b], and Boaz Pokroy[a,b,1]

Edited by Lia Addadi, Weizmann Institute of Science, Rehovot, Israel; received November 4, 2021; accepted March 13, 2022

During the process of biomineralization, organisms utilize various biostrategies to enhance the mechanical durability of their skeletons. In this work, we establish that the presence of high-Mg nanoparticles embedded within lower-Mg calcite matrices is a widespread strategy utilized by various organisms from different kingdoms and phyla to improve the mechanical properties of their high-Mg calcite skeletons. We show that such phase separation and the formation of high-Mg nanoparticles are most probably achieved through spinodal decomposition of an amorphous Mg-calcite precursor. Such decomposition is independent of the biological characteristics of the studied organisms belonging to different phyla and even kingdoms but rather, originates from their similar chemical composition and a specific Mg content within their skeletons, which generally ranges from 14 to 48 mol % of Mg. We show evidence of high-Mg calcite nanoparticles in the cases of six biologically different organisms all demonstrating more than 14 mol % Mg-calcite and consider it likely that this phenomenon is immeasurably more prevalent in nature. We also establish the absence of these high-Mg nanoparticles in organisms whose Mg content is lower than 14 mol %, providing further evidence that whether or not spinodal decomposition of an amorphous Mg-calcite precursor takes place is determined by the amount of Mg it contains. The valuable knowledge gained from this biostrategy significantly impacts the understanding of how biominerals, although composed of intrinsically brittle materials, can effectively resist fracture. Moreover, our theoretical calculations clearly suggest that formation of Mg-rich nanoprecipitates greatly enhances the hardness of the biomineralized tissue as well.

biomineralization | high-Mg calcite | nanoprecipitates | spinodal decomposition

Significance

Biominerals are extraordinarily intricate and possess superior mechanical properties compared with their synthetic counterparts. In this study, we show that the presence of high-Mg calcite nanoparticles within a low-Mg calcite matrix is a widespread phenomenon among marine organisms whose skeletons are composed of high-Mg calcite. It seems most likely that formation of such a complex structure is possible because of the phase separation that occurs as a result of spinodal decomposition of an amorphous Mg–calcium carbonate precursor and is followed by crystallization. We demonstrate that the basis of such phase separation stems from chemical composition rather than from biological similarities. The presence of high-Mg calcite nanoparticles increases the skeletons' toughness and hardness.

A range of organisms utilizes calcite to build their skeletons while incorporating Mg into the crystal lattice (1–5). The content of Mg within the calcite crystal varies (6), from as low as only a few moles percentage to levels as high as 45 mol % (7, 8). High-Mg calcite biominerals with a Mg content that exceeds the thermodynamic solubility limit are secreted by a wide variety of organisms belonging to different kingdoms and phyla. For example, high-Mg calcite is found in the skeletons of brittle stars (9), sea urchins (10), starfish (11), sea sponges (12), and corals (13) as well as in plants such as the coralline red algae (14, 15). The Mg plays a significant role in the crystallization process (16–18), and the incorporation of large amounts of Mg is facilitated by crystallization via an amorphous calcium carbonate (ACC) precursor (19–23). The incorporated Mg ions modulate the crystal properties of the $CaCO_3$, enhancing its structural performance. Owing to the smaller radii of Mg ions than those of Ca ions (24), compressive stresses are formed within the $CaCO_3$ crystal and lead to improved hardness (25, 26).

The brittle star *Ophiomastix wendtii* (9, 27) and two species of the coralline red algae, *Jania* sp. and *Corallina* sp. (28), were the focus of our recent studies on high-Mg calcite biomineralization. The brittle star *O. wendtii* (phylum Echinodermata) is an echinoderm that is highly sensitive to light and possesses a remarkable visualization system composed of micrometer-sized Mg-calcite lenses located on its dorsal arm plates, all directed along their *c* axis upright to avoid birefringence (29, 30). *Jania* sp. and *Corallina* sp. (phylum Rhodophyta) are highly abundant coralline red algae growing in oceans worldwide (31). When residing in shallow waters, they are constantly exposed to external stresses imposed by the sea waves (32, 33). These algae incorporate hollow helical microstructures that highly increase their compliance, allowing them to better adapt to their natural environment (34). They are heavily mineralized, with Mg-calcite nanocrystals deposited on their cell walls (35–37). Despite their biological distinction, these three organisms demonstrate common structural aspects, among which is the presence of high-Mg nanoparticles embedded within the lower-Mg calcite matrices of their skeletons. An earlier study of *O. wendtii* by our group revealed that the high-Mg nanoparticles are coherently aligned within the lenses' low-Mg calcite matrix and are

Author affiliations: [a]Department of Materials Science and Engineering, Technion–Israel Institute of Technology, 32000 Haifa, Israel; [b]The Russell Berrie Nanotechnology Institute, Technion–Israel Institute of Technology, 32000 Haifa, Israel; and [c]ID22, European Synchrotron Radiation Facility –The European Synchrotron, Grenoble cedex 9, 38043 France

Author contributions: N.B.-S., I.P., A.K., and B.P. designed research; N.B.-S., I.P., A.L., L.P., and C.D. performed research; N.B.-S. and A.L. analyzed data; B.P. supervised the research; and N.B.-S., I.P., A.K., and B.P. wrote the paper.

The authors declare no competing interest.

This article is a PNAS Direct Submission.

[1]To whom correspondence may be addressed. Email: bpokroy@technion.ac.il.

This article contains supporting information online at http://www.pnas.org/lookup/suppl/doi:10.1073/pnas.2120177119/-/DCSupplemental.

Published April 11, 2022.

distributed in alternating layers of varying densities (9). We also observed similar structural organization in other skeletal parts of *O. wendtii*, specifically its spicules, arm vertebrae, and teeth (27). In the case of both coralline red algae species, we found that the high-Mg nanoparticles were located within the poor-Mg hosting nanocrystal matrices and in contrast to the brittle star *O. wendtii*, that they were included noncoherently (28). Additionally to our results, previous reports on the red coral *Corallium rubrum* also described Mg-calcite nanodomains within its skeleton, but they were not specified as high-Mg calcite nanoparticles (38).

Based on calculations, we proposed (27) that the formation of high-Mg nanoparticles in *O. wendtii* originates from the spinodal decomposition of a Mg–ACC precursor and showed that such decomposition takes place in the nonstable region with a Mg content in the range of 14 to 48 mol %. This model was subsequently used by our group to explain the possible mechanism of formation of the high-Mg nanoparticles found in the coralline red algae (28). However, as we can only study the final mineralized tissue, we cannot completely rule out other formation mechanisms, although we believe that this is unlikely. Layered structures were observed in both *O. wendtii* and *Jania* sp. and were related to alternating concentrations of high-Mg nanoparticles in the layers, which were explained as probably a result of secondary spinodal decomposition (27, 28).

In all of the above organisms studied, regardless of the biological and morphological differences between them, the presence of high-Mg calcite nanoparticles led to enhanced fracture resistance. The use of hierarchical structures to enhance mechanical properties is a well-known strategy exploited in nature by various organisms (39–44). Based on our earlier findings, we envisaged that the inclusion of high-Mg nanoparticles within Mg-calcite crystals is a widespread strategy in nature, serving pivotal structural roles in enhancing the mechanical properties of the biomineralized tissue.

In the present study, we now generalize this biostrategy and confirm its widespread prevalence in high-Mg calcite biomineralization. We show that yet another common and relatively small brittle star (45) *Ophiactis savignyi* as well as the soft coral *Tubipora musica* (also known as the organ pipe coral) and the starfish *Echinaster sepositus* show evidence of high-Mg nanoparticles dispersed within a low-Mg calcite matrix. We carried out an extensive comparative study, which yielded fundamental insights into the similarities and differences in structure between the different organisms. Based on this study, we can strongly suggest that spinodal decomposition is probably a general and most likely precrystallization step preceding the formation of high-Mg nanoparticles occurring in biomineralized tissues of organisms across different kingdoms and phyla and that the specific chemical composition of the organism's skeletons is the basis for this phenomenon. The results of this study can be expected to profoundly affect the understanding of the biomineralization process and the mechanisms utilized by organisms to improve their mechanical endurance.

Results

This research was focused on a broad comparative study of the structure of a variety of organisms across different kingdoms and phyla. The following organisms included in the animal kingdom but classified among different phyla were selected: the brittle star *O. savignyi* (phylum Echinodermata), the soft coral *T. musica* (also known as the organ pipe coral; phylum Cnidaria), and a starfish *E. sepositus* (phylum Echinodermata). In addition, for the purpose of generalization, we include into the discussion the data we previously obtained from two coralline red algae species belonging to the plant kingdom, *Jania* sp. and *Corallina* sp., and from the brittle star *O. wendtii* (phylum Echinodermata). Fig. 1 displays the different organisms (Fig. 1, *Insets*) and their microstructures imaged using high-resolution scanning electron microscopy (HRSEM). It is apparent from the images that the organisms are highly diverse. The brittle star *O. wendtii* (Fig. 1*A*) has five arms and a body of ∼1.5 cm, while *Jania* sp. and *Corallina* sp. (Fig. 1 *B* and *C*) are branched articulated algae composed of calcified joints and interconnecting segments. The brittle star *O. savignyi* (Fig. 1*D*) also possesses five arms, but its body dimension of ∼0.5 cm is smaller than that of *O. wendtii*. The skeleton of *T. musica* (Fig. 1*E*) is arranged in hollow tubes with a diameter of ∼0.2 cm and interconnecting horizontal platforms. The starfish *E. sepositus* (Fig. 1*F*) possesses five arms. Microstructures of the mineralized tissues of the six organisms also differ significantly. Whereas *Jania* sp. and *Corallina* sp. possess nanometric-sized crystals deposited on the cell walls (*SI Appendix*, Fig. S1), the crystalline features of the four other organisms are micrometric in size. The two coralline red algae have nanocrystals of similar dimensions. On the other hand, the crystalline features in the two brittle stars are different; the lenses of *O. wendtii* are typically 20 to 50 μm in size, whereas the features of *O. savignyi* are significantly smaller and are in the range of a few micrometers. Exceptional to all other organisms is *T. musica*, whose microstructure is significantly less porous.

Energy-dispersive X-ray spectroscopy (EDS) analysis of the samples confirmed the presence of Mg in the studied organisms (*SI Appendix*, Fig. S2). We further analyzed the samples via inductively coupled plasma optical emission spectroscopy (ICP-OES) to accurately measure the average Mg content in *O. savignyi*, *T. musica*, and *E. sepositus* (*SI Appendix*, Table S1). As expected, the Mg content is relatively high and in the range of 15.35 to 15.51 mol % [calculated based on the ratio of Mg/(Ca + Mg)].

Mineralized tissues of each organism were studied in powdered form using synchrotron high-resolution powder X-ray diffraction (HRPXRD). The collected full-diffraction patterns presented in Fig. 2*A* confirmed that all skeletons possess the crystalline structure of calcite. As represented by the {104} diffraction peak in Fig. 2*B*, the diffraction peaks are shifted to higher 2θ angles relative to those of pure calcite. This shift is mainly a result of substitution of Mg ions, with their smaller ionic radii, for Ca ions in the calcite lattice (24). As expected and owing to Mg substitution, lattice parameters extracted using the Rietveld refinement are smaller than those of pure calcite (*SI Appendix*, Table S2). It is also possible that the shift of the diffraction peaks is a result of additional stresses in the crystals. A prominent difference is observed in the width of the {104} diffraction peak of the different organisms, with a broader diffraction peak in the case of *Jania* sp. and *Corallina* sp., which can be related to the nanometric size of their crystals (Fig. 1 *B* and *C*).

Employing high-resolution transmission electron microscopy (HRTEM) disclosed the presence of high-Mg nanoparticles dispersed within the Mg-calcite matrices of the brittle star *O. savignyi*, the coral *T. musica*, and the starfish *E. sepositus*, even though all of these three mineralized tissues diffracted as single crystals under transmission electron microscopy (TEM) (Fig. 3). Fig. 3*A* presents an HRTEM image of a lamella of the brittle star *O. savignyi* acquired using a high-angle annular dark

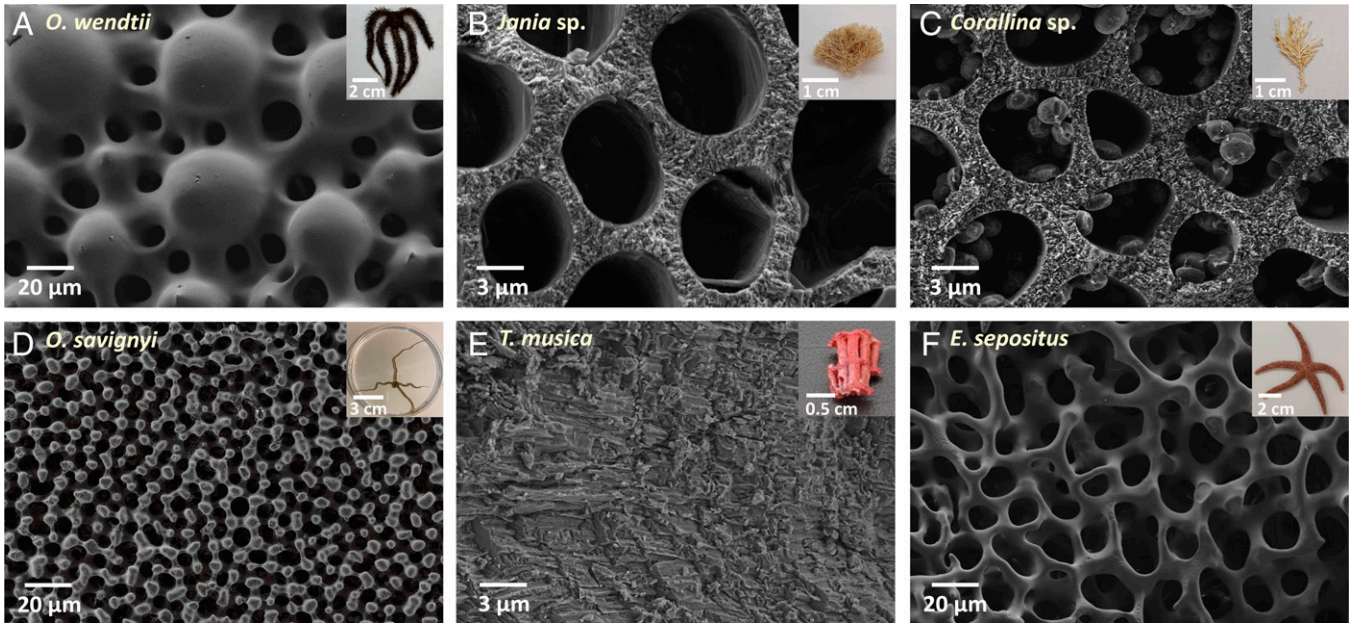

Fig. 1. Microstructures of the different organisms imaged using HRSEM. (*A*) *O. wendtii*. (*B*) *Jania* sp. (*C*) *Corallina* sp. (*D*) *O. savignyi*. (*E*) *T. musica*. (*F*) *E. sepositus*. The different organisms are presented in *Insets* in *A*–*F*.

field (HAADF) detector and reveals nanoparticles displaying a darker contrast than that of the matrix. Owing to the sensitivity of the HAADF detector to changes in atomic number, this result indicates that the nanoparticles are composed of lighter elements than those of the hosting matrix. Combining this result with data from EDS again paints a picture of nanoparticles composed of Mg-calcite with a higher Mg content than that of the matrix. The nanoparticles, similarly to our previous findings on the high-Mg nanoparticles found in the brittle star *O. wendtii* (27), are arranged in layers. Although the presence of nanoparticles is evident within the matrix, the diffraction pattern of *O. savignyi* is that of a single crystal (Fig. 3 *A*, *Inset*). Examination of a lamella of the coral *T. musica* using HRTEM presents the same phenomenon (Fig. 3*B*). Crystalline nanoparticles are present within the Mg-calcite matrix and according to the phase-contrast image, possess various crystallographic orientations (i.e., they are incoherent with the hosting matrix). This is even though a large area of the sample containing both the matrix and the nanoparticles diffracts as a single crystal (Fig. 3 *B*, *Inset*). The starfish *E. sepositus* also exhibits nanoparticles, although the diffraction shows a spot diffraction pattern from a large area. The nanoparticles are coherent with the hosting matrix since both the matrix and the nanoparticles present a continuous pattern in phase-contrast HRTEM (Fig. 3*C*).

The presence of nanoparticles within the lattice of these three organisms was also supported here by the results of isochronous annealing experiments coupled with synchrotron radiation HRPXRD. By means of this method, the appearance of an additional broad diffraction peak after heating to 400 °C and its correlation to the nanoparticles' phase had been established in *O. wendtii* (9). Powdered samples of these three organisms were heated to various temperatures and measured using synchrotron radiation HRPXRD at room temperature after the samples had cooled. The findings obtained in the new species were akin to the earlier observations in *O. wendtii*, *Corallina* sp., and *Jania* sp. We found that after heating a sample of the brittle star *O. savignyi* ex situ in air to 400 °C, a new broad diffraction peak appeared at higher 2θ angles (Fig. 3*D*) at a position corresponding to calcite with ∼42 mol % Mg. The same was detected for the coral *T. musica* but only after its

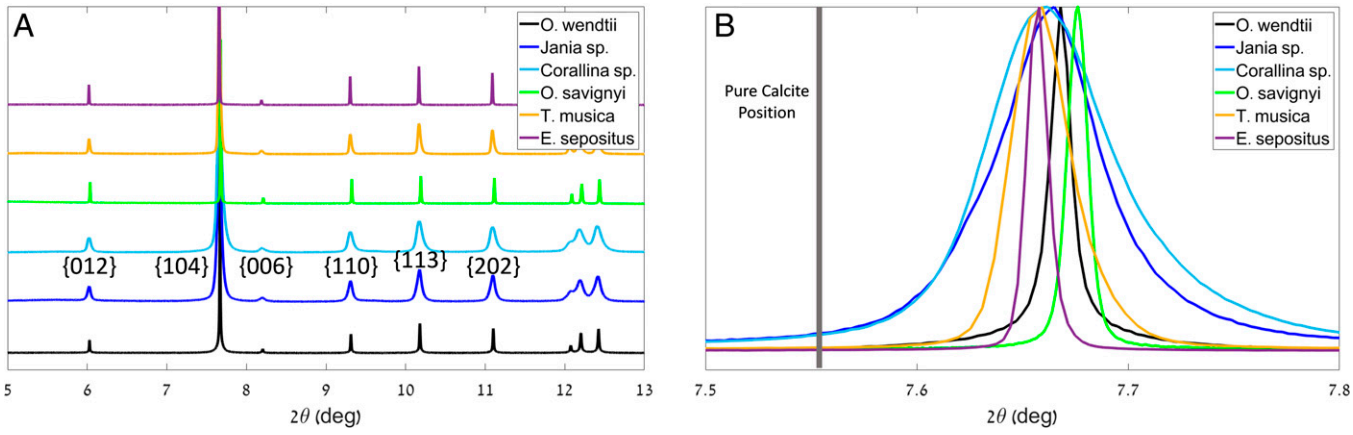

Fig. 2. Synchrotron radiation HRPXRD data. (*A*) HRPXRD patterns of the mineralized tissues of the studied organisms showing their crystalline calcite structures. The data were collected at a wavelength of 0.4 Å. (*B*) Mg calcite {104} diffraction peaks of the studied organisms relative to the {104} position of the pure calcite.

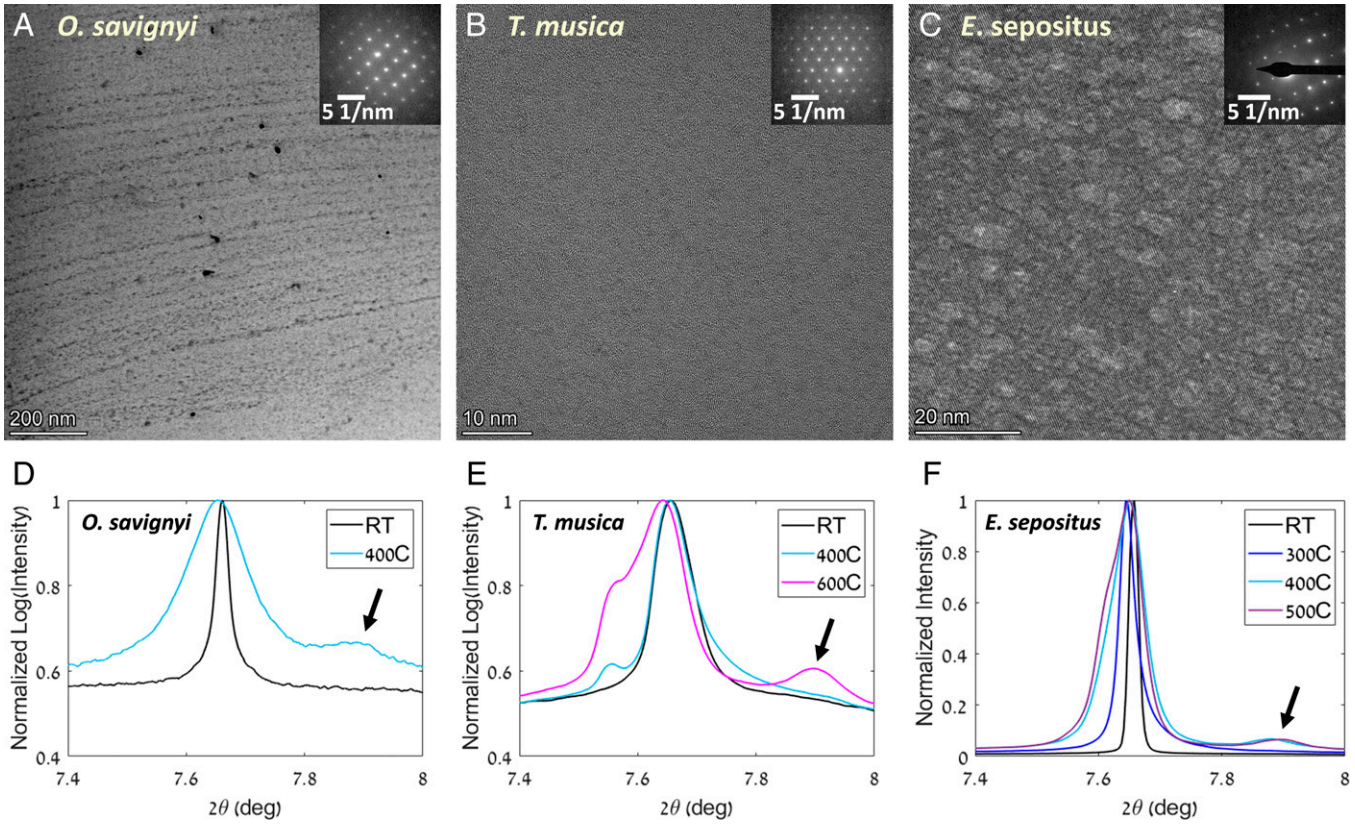

Fig. 3. HRTEM and synchrotron radiation HRPXRD results. (*A*) HRTEM image of *O. savignyi* acquired using an HAADF detector. (*B*) HRTEM image of *T. musica* showing incoherent nanoparticles. (*C*) HRTEM image of *E. sepositus* showing coherent nanoparticles. (*Insets* in *A*–*C*) Diffractions from regions containing the matrix as well as the nanoparticles in the studied organisms. HRPXRD results show the evolution of the {104} diffraction peak of Mg-calcite after heating presented for a wavelength of 0.4 Å: (*D*) *O. savignyi*, (*E*) *T. musica*, and (*F*) *E. sepositus*. RT, room temperature.

heating ex situ in air to the higher temperature of 600 °C (Fig. 3*E*). The Mg content related to the new diffraction peak was estimated as ∼44 mol % Mg. In the case of the starfish *E. sepositus*, the new diffraction peak appeared at a temperature of 400 °C in air, which corresponds in position to a Mg content of ∼41 mol % Mg (Fig. 3*F*).

Both the HRTEM and HRPXRD results confirmed that these three organisms, despite the fact that biologically they are highly diverse, include high-Mg nanoparticles within their matrices composed of Mg-calcite with a lower-Mg content. When we combine these results with our previous findings related to the brittle star *O. wendtii* and the coralline red algae *Jania* sp. and *Corallina* sp., it is clear that all these mineralized tissues not only contain high-Mg nanoparticles within their Mg-calcite matrices but interestingly, all exhibit a total Mg content of over 14 mol %. We previously showed via thermodynamic theoretical calculations that Mg–ACC is thermodynamically unstable in Mg concentration in the range from 14 to 48 mol %. Moreover, we showed, that this instability has high prospects to result in a spinodal decomposition to a lower-Mg matrix and higher-Mg phases (27). Those calculations as well as the fact that Mg-calcite with Mg concentrations above a few percent can only be formed via ACC, combined with the current widespread finding of such Mg-rich nanoparticles within a low-Mg matrix, allow us to hypothesize that probably the formation of high-Mg nanoparticles took place in the amorphous stage prior to crystallization via spinodal decomposition.

To further verify this hypothesis, we selected three other biomineralized tissues, which exhibit rather high but lower than the 14 mol % average Mg content (lower limit of the instability gap). To this end, spines of the sea urchins *Phyllacanthus imperialis*, *Paracentrotus lividus*, and *Heterocentrotus mammillatus* (phylum Echinodermata) were selected for this study. ICP-OES indeed revealed a substantially lower Mg content in the range of 4.11 to 10.63 mol % (*SI Appendix*, Table S1).

HRPXRD performed on powdered samples of the three lower–Mg content tissues, as expected, did not demonstrate the emergence of an additional broad diffraction peak upon isochronous annealing, even in a high-pressured CO_2 environment under which the decomposition of Mg-calcite to Mg-calcite with a lower Mg content, MgO, and CO_2 at elevated temperatures is retarded (*SI Appendix*, Fig. S3). These observations allowed us to rule out the presence of high-Mg nanoparticles within the matrices of the biomineralized tissues of *P. imperialis*, *P. lividus*, and *H. mammillatus*.

Fig. 4 depicts the various studied biomineralized tissues according to the measured Mg content via ICP-OES and indicates whether high-Mg nanoparticles exist or not. It is evident that high-Mg nanoparticles are present only for those tissues that exhibit an average Mg content above 14 mol %.

We believe that the high-Mg nanoparticles existing within the different biomineralized tissues may serve a critical functional role in the mechanical properties of these organisms. They contribute to an increased fracture toughness and increased crack resistance of the organisms' skeletons, which in turn, enable the organisms to withstand external stresses and possible dangers from their natural environment (9, 28, 34). In addition, it is reasonable to assume that high-Mg nanoparticles also increase the total hardness of the inhomogeneous Mg-calcite structure. The enhanced hardness of biogenic calcite compared with that of geological calcite is usually attributed to solid-solution strengthening due to substitution of Ca^{2+} by

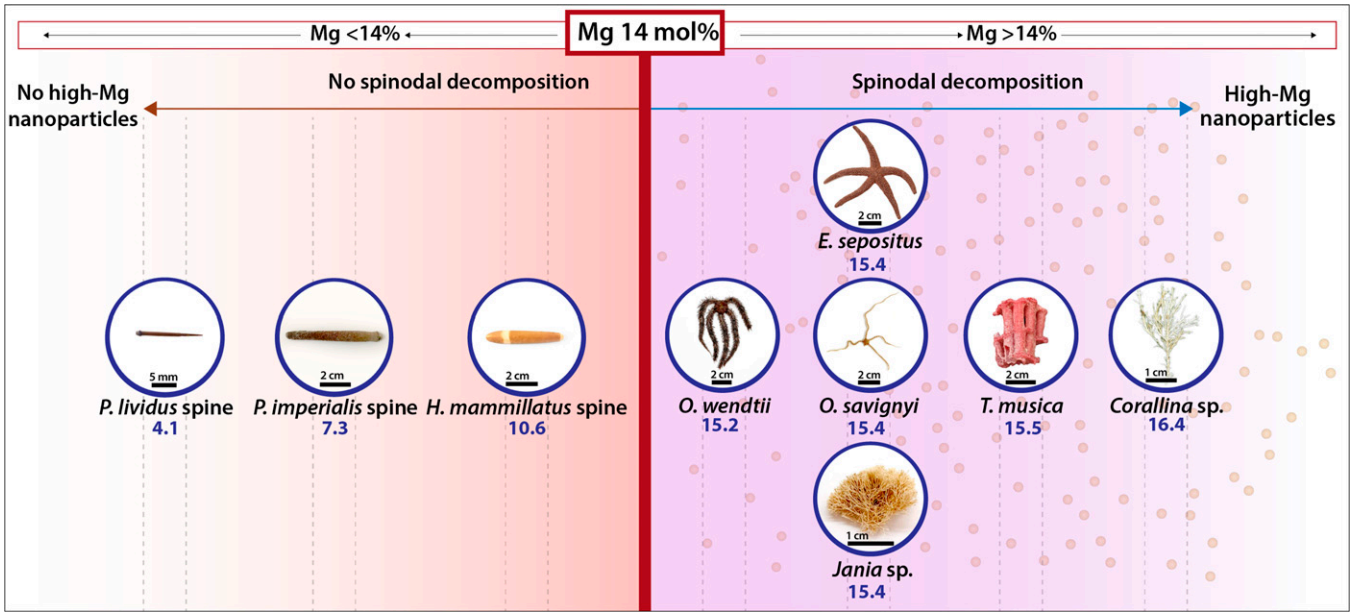

Fig. 4. The various studied biomineralized tissues divided into two categories based on their Mg content. High-Mg nanoparticles are present only for those with an average Mg content higher than 14 mol %.

Mg^{2+}in the calcite crystal structure (46). However, the formation of the inhomogeneous Mg-calcite nanostructure may result in additional strengthening caused by the interaction between the nanoparticles and dislocations (precipitation hardening). It was shown that nanoprecipitates can be either sheared or bypassed by moving dislocations depending on the size, coherency, and spacing of the nanoprecipitates (47). The stress at which the nanoprecipitates are overcome during shearing is proportional to their average size and is inversely proportional to the average distance between them. This stress can be written as follows (48):

$$\sigma_{shear} \simeq 1.15\tilde{\Gamma}\sqrt{\frac{3f_v\bar{R}_p}{2\pi}}, \qquad [1]$$

where f_v is the volume fraction of the nanoprecipitates, $\bar{R}_p$ is the average nanoprecipitates radius, $\tilde{\Gamma} = \Gamma_1^{3/2}(b/2\Gamma)^{1/2}$, $\Gamma_1 = 2\gamma_a/b$, and γ_a represents the counter dislocation motion force per unit length as the dislocations penetrate the nanoprecipitates, whereas b is the Burgers vector. Assuming $\gamma_a = \alpha G_p b$, where α is a numerical parameter that depends on the nanoprecipitates geometry [for a spherical precipitate of radius R, it can be estimated as $\alpha \approx 1.4(b/R)$] (*SI Appendix*, note I), and $\Gamma \approx Gb^2$ is the dislocation line tension, where G and G_p are the shear moduli of the calcite matrix and of the Mg-rich nanoprecipitates, respectively, one can rewrite Eq. **1** as $\sigma_{shear} \simeq 2.3\alpha^{3/2}G_p\sqrt{\frac{3f_v\bar{R}_pG_p}{2\pi bG}}$. Using the reasonable values $b = 0.8$ nm, $\bar{R}_p = 8$ nm, $f_v = 0.08$, $G = 37$ GPa, and $G_p = 41$ GPa (as for Mg-calcite with 40 mol % of Mg) (9, 49) yields $\sigma_{shear} \simeq 3.2$ GPa.

As a next step, we estimate the stresses needed to cause a dislocation to bypass nanoprecipitates on the glide plane. According to the Orowan equation (48, 50, 51),

$$\sigma_{bypass} = 1.4\frac{Gb}{\bar{R}_p}\sqrt{\frac{3f_v}{2\pi}}. \qquad [2]$$

Incorporating reasonable values for this system of $G = 37$ GPa, $b = 0.8$ nm, $\bar{R}_p = 8$ nm, and $f_v = 0.08$ yields $\sigma_{bypass} \simeq 1.0$ GPa. Owing to the size distribution of the nanoprecipitates, both shearing and bypassing precipitation strengthening mechanisms can operate simultaneously. It was shown via both computer simulations (51) and theoretical calculations (52) that the Pythagorean addition rule demonstrates the best approximation in the case where the two precipitation strengthening mechanisms operate in parallel:

$$\Delta\sigma_{prec} = \sqrt{(\sigma_{shear})^2 + (\sigma_{bypass})^2}. \qquad [3]$$

Therefore, the precipitation hardening can be estimated as $\Delta\sigma_{prec} \simeq \sqrt{(3.2)^2 + (1.0)^2} = 3.35$ GPa.

It is interesting to compare this obtained value with that of the solid-solution strengthening caused by Mg atoms homogeneously distributed in the calcite matrix. The solid-solution strengthening has been experimentally studied by Kunitake et al. (26) for small Mg concentrations, namely less than 1 mol % via indentation experiments. Their results can be equally fitted by both linear and square root dependences; in the latter case, they can be approximated as $\Delta H_{ss} = \Delta H_0 X^{0.5}$, where X is the atomic Mg concentration, with $\Delta H \approx (6 \div 11)$ GPa, depending on the indentation direction. Extrapolation to higher Mg concentrations of ~15 mol % would result in strengthening by $\Delta H_{ss} = (2 \div 4)$ GPa.

One can suggest that the hardening observed in biogenic calcite containing a heterogeneous distribution of Mg-rich nanoprecipitates within a Mg-calcite matrix is a result of the combined effect of solid-solution strengthening and precipitation hardening, while the latter mechanism alone enhances the hardening at least by twofold. Indeed, this was confirmed by the study of Polishchuk et al. (9), where the hardness of a (001)-oriented calcite single crystal with coherently aligned Mg-rich nanoprecipitates (with average Mg concentration of 15.2 ± 0.1 mol %) was found to be as high as 7.46 ± 1.62 GPa. For comparison, the hardness of (001)-oriented geological calcite was shown to be only (2.30 to 2.5) GPa, and that of biogenic low Mg-calcite is only (3.5 to 4.2) GPa. It should be noted that precipitation of Mg-rich nanoprecipitates decreases the average Mg concentration in a Mg-calcite matrix and thus, diminishes the corresponding solid-solution strengthening effect. However,

the decrease in Mg concentration of the matrix in the studied cases is rather small (for example, from 15 to 13 mol % in the brittle star *O. wendtii*), so the decrease of the solid-solution strengthening effect is minor compared with the increase in hardness due to the formation of nanoprecipitates. The latter is not surprising as it is known in classical metallurgy that impurities existing as coherent or incoherent nanoprecipitates are more effective in impeding the movement of dislocations compared with the effect of impurities in solid solutions. In addition, in some metallurgical systems, it is reported that precipitation leads to a much greater strengthening of a matrix compared with the effect of solid-solution strengthening (53).

Discussion

The findings of this research on the structure of biomineralized tissues in the nine selected organisms clearly prove that the presence of high-Mg calcite nanoparticles within a low-Mg calcite matrix is a widespread phenomenon in high-Mg calcite biological systems. The fact that high-Mg nanoparticles are selectively present within the different species even of the same phylum (as shown here for the studied brittle stars compared with the studied sea urchins, which are all echinoderms) is a strong indication that this phenomenon is not related to biological similarities between species but can rather be attributed to the compositional similarities of their mineralized tissues and specifically, to the Mg content.

As proposed in our previous study (27), the high-Mg nanoparticles in *O. wendtii* are formed via spinodal decomposition of the Mg–ACC precursor. Generally, spinodal decomposition was shown to be enabled when the Mg content in the calcite is in the range of 14 to 48 mol % (i.e., in high-Mg calcite systems). Given the high contents of Mg [exceeding the thermodynamically stable limit of Mg within calcite at room temperature, which is on the order of only a few moles percentage (2)] incorporated within the calcitic skeletons studied herein and owing to the intricate microstructures found in these organisms, it is reasonable to suggest that their crystallization followed from a Mg–ACC precursor, as was previously stated for many biominerals, among them *O. wendtii*, *Jania* sp., and *Corallina* sp. (9, 20, 28, 54–56). The present detection of high-Mg nanoparticles in *O. savignyi*, *T. musica*, and *E. sepositus* and the fact that their skeletons all include Mg contents within a range that allows spinodal decomposition are strong indications that the formation of high-Mg nanoparticles within Mg-calcite crystals very possibly follows spinodal decomposition of a Mg–ACC precursor and is a widespread phenomenon that is not limited to specific organisms. This is further supported by the fact that in those organisms in which the Mg concentration is lower than 14 mol % (out of the instability gap), no such nanoparticles exist. Of course, we cannot rule out another route of nanoparticles formation, namely their precipitation during crystallization, as we are studying the final mineralized tissue and not able to follow their formation in situ.

The occurrence of spinodal decomposition is conditional on the rate of the Mg and Ca ions diffusion, which is too slow in solid Mg-calcites under ambient conditions, while it can be fast enough in liquids and gels. That is why we propose that the spinodally decomposed matrix is a Mg–ACC gel or liquid-like phase, which is thermodynamically akin to the corresponding crystalline solution. The second possible route of the Mg-rich nanoparticles precipitation in this Mg concentration range via a nucleation and growth pathway is much slower than spinodal decomposition since it requires multiple nucleation events, while spinodal decomposition becomes initiated in the absence of any nucleation and may result from minor fluctuations in composition. Thus, combining the fact that spinodal decomposition is faster and is favorable thermodynamically for a Mg concentration in the range of 14 to 48 mol % together with the fact that nanoparticles are found only in those organisms that demonstrate Mg levels within that range strongly supports the possibility that indeed spinodal decomposition took place prior to crystallization. Additionally, our observation that in several organisms in which nanoparticles were found, we also observe their organization in layers with alternating concentrations (as seen for the brittle stars *O. wendtii* and *O. savignyi* and for the alga *Jania* sp.) is an additional indication that strengthens the spinodal decomposition scenario, as was explained in detail in our previous work (27). Despite the above considerations in favor of the spinodal decomposition scenario, the authors cannot unquestionably rule out the route via nucleation and growth.

Other formation scenarios of a layered structure with fluctuation in the total Mg concentration can be envisaged, such as a solution-based equivalent of constitutional supercooling driven by the exclusion of Mg atoms from crystallizing calcite. The Mg concentration within the solid solution can vary with the fluctuations in the crystallization rate as was suggested by Haase et al. (57) and Allegre et al. (58) to explain the oscillatory zoning in plagioclase feldspar. A reason for such fluctuations in the calcite crystallization rate can be the accumulation of the excluded Mg ions within the Mg–ACC ahead of the crystallization front, which promotes a decrease in the crystallization rate. The trend toward a decrease in the crystallization rate can be reversed upon spinodal decomposition of the Mg–ACC layer adjacent to the crystallization front. However, excessive Mg excluded from the calcite matrix during crystallization is then accumulated in additional Mg-rich nanoparticles incorporated into the calcite matrix. The latter effect is probably dominant in variation of the Mg concentration in the considered two-phase structure.

Examination of all studied species shows that there is a clear difference in the arrangement of the nanoparticles found within them. The nanoparticles in the brittle star *O. wendtii* (9) and the starfish *E. sepositus* (present study) are coherent with the hosting matrix. The nanoparticles in *Jania* sp. (28), *Corallina* sp. (28), and *T. musica* (present study) are incoherent with the hosting matrix. The coherence between a low-Mg calcite matrix and numerous Mg-rich calcite nanoprecipitates is observed within single crystals. This can be explained by crystallization from a single nucleation event, proceeding in the low-Mg-ACC matrix. A possibility that can explain the noncoherence of the nanoparticles containing higher Mg levels is that during crystallization (which will start from the lower-Mg content matrix), only the low-Mg matrix crystallizes, and the high-Mg nanodomains do not crystallize at first, as the higher Mg concentration stabilizes the amorphous state. Then, at a later stage, at some point the amorphous nanodomains undergo nucleation and growth in different crystallographic orientations than that of the matrix. Another possibility for the incoherency is the slightly higher Mg content, thus a larger lattice mismatch, within those species containing the noncoherent nanoparticles. In such a case, the coherency loss can occur due to the size of Mg-rich particles exceeding a critical size (59).

The HRPXRD results indicate a decreased thermal stability for the high-Mg nanoparticles found within the coralline red algae relative to the other studied organisms. A possible reason for this could be the different length scales of the hosting

matrix crystals, which are micrometric in *O. wendtii*, *O. savignyi*, *T. musica*, and *E. sepositus*, whereas in the two studied coralline red algae, they are nanometric. Their nanometric size in the red algae could possibly be attributable to a high nucleation rate, which might also result in a noncoherent arrangement of the nanoparticles.

In regard to the implications of the presence of the high-Mg nanoparticles within a low-Mg matrix on the mechanical properties, it is clear from our calculations in this paper that their presence strongly enhances not only the fracture toughness but also, the hardness of the mineralized tissue. The fact that lowering the concentration of Mg in the matrix by only 1 to 2 mol % in order to form the high-Mg nanoparticles enhances the hardness by 100% is a fascinating finding. This biostrategy not discussed previously in the literature really presents a minimal energy and facile route to enhancing the mechanical properties.

To conclude, the inclusion of high-Mg calcite nanoparticles within a low-Mg calcite matrix identified in six biologically distinct organisms demonstrating more than 14 mol % Mg-calcite is shown to be widespread. We believe that it is very likely that this phenomenon is even more widespread in biomineralization. We propose that the formation of the high-Mg nanoparticles is most likely achieved through spinodal decomposition of a Mg–ACC precursor and show that their existence has a functional and mechanical role. This unique and previously unidentified biomineralization strengthening strategy of high-Mg nanoparticles inclusion is of great importance in the field of materials science, with special emphasis on the design of high-performance tough materials.

Materials and Methods

Sample Collection. Samples of *O. wendtii* were collected in Belize. Samples of *Jania* sp. and *Corallina* sp. were collected from the shallow waters of the Mediterranean Sea, Israel. Samples of *O. savignyi* were collected from the Red Sea, Israel. Samples of *T. musica* were collected in Zanzibar. Samples of the starfish *E. sepositus* were collected from the Mediterranean Sea, Israel. Samples of *P. imperialis* and *H. mammillatus* were collected in the Philippines. Samples of *P. lividus* were supplied by the Israel Oceanographic and Limnological Research Institute.

Sample Bleaching. Samples of *O. wendtii* and *E. sepositus* were bleached for the removal of organic matter in deionized (DI) water and sodium hypochlorite (NaOCl) solution with a 2:1 volume ratio of NaOCl/DI for 8 and 2 h, respectively. Sodium carbonate (2 wt %) was added to the DI water to avoid dissolution of calcite. After bleaching of the organics, the mineralized samples were washed several times with DI and dried in air.

HRSEM. Microstructures of the six studied organisms were examined by HRSEM using a Zeiss Ultra-Plus FEG-SEM with a secondary electron detector and acceleration voltages of 4 kilovolts (kV). Prior to measurement, the samples were coated with carbon.

EDS. EDS was performed using an Oxford Silicon Drift Detector EDS installed in a Zeiss Ultra-Plus FEG-SEM with an acceleration voltage of 10 kV.

HRPXRD. Samples of *O. wendtii*, *Jania* sp., and *Corallina* sp. were measured by synchrotron radiation HRPXRD at the ID22 beamline of the European Synchrotron Radiation Facility (ESRF) in Grenoble, France using a wavelength of 0.3999 Å at room temperature. Samples of *O. savignyi* were measured using synchrotron radiation HRPXRD at the 11BM-B beamline at the Advanced Photon Source at the US Department of Energy's Argonne National Laboratory (Illinois) using a wavelength of 0.4579 Å. Heating was performed ex situ at 400 °C for 30 min, and the sample was later measured at room temperature after heating. Samples of *T. musica* were measured using synchrotron radiation HRPXRD at the ID22 beamline of the ESRF in Grenoble, France using a wavelength of 0.3545 Å. Heating was performed ex situ at 400 °C and 600 °C for 30 min, and the samples were later measured at room temperature after heating. A sample of *E. sepositus* was measured using synchrotron radiation HRPXRD at the ID22 beamline of the ESRF in Grenoble, France using a wavelength of 0.3542 Å. Isochronous annealing was performed to temperatures of 300 °C, 400 °C, and 500 °C for 30 min. A sample of *P. imperialis* was measured using synchrotron radiation HRPXRD at the ID22 beamline of the ESRF in Grenoble, France in a high-pressured CO_2 environment (∼20 atmospheres) using a wavelength of 0.3542 Å. Isochronous annealing was performed to temperatures of 400 °C, 500 °C, and 600 °C for 30 min. A sample of *P. lividus* was measured using synchrotron radiation HRPXRD at the ID22 beamline of the ESRF in Grenoble, France in a high-pressured CO_2 environment (∼15 atmospheres) using a wavelength of 0.3542 Å. Isochronous annealing was performed to temperatures of 400 °C, 500 °C, and 600 °C for 30 min. A sample of *H. mammillatus* was measured using synchrotron radiation HRPXRD at the ID22 beamline of the ESRF in Grenoble, France in a high-pressured CO_2 environment (∼30 atmospheres) using a wavelength of 0.3542 Å. Isochronous annealing was performed to temperatures of 500 °C and 600 °C for 30 min.

HRTEM. The FEI Titan Cubed Themis G2 60–300 was operated at 200 KV for the study of a focused ion beam (FIB)-sectioned lamella of *O. savignyi* in scanning-transmission electron microscopy mode using an HAADF detector and at 60 KV for its study in TEM mode. The FEI Titan Cubed Themis G2 60–300 was operated at 60 and 200 KV for the study of a plasma FIB-sectioned *T. musica* lamella in TEM mode. An FIB-sectioned lamella of *E. sepositus* was studied using the FEI Titan Cubed Themis G2 60–300 operated at 60 KV in TEM mode.

ICP-OES. ICP-OES was performed using an iCAP 6300 Duo ICP-OES spectrometer (Thermo Scientific). Prior to measurements, the samples were weighed and fully dissolved in HNO_3.

Data Availability. All study data are included in the article and/or *SI Appendix*.

ACKNOWLEDGMENTS. We acknowledge the ID22 beamline at the ESRF (Grenoble, France) and the 11BM-B beamline at the Advanced Photon Source at the US Department of Energy's Argonne National Laboratory (Illinois) for assisting in collection of HRPXRD data. We thank Dr. Gordon Hendler, Prof. Giuseppe Falini, Dr. Tali Mass, and Dr. Boaz Mayzel for sample collection. This research was partly funded by the European Research Council (ERC) under the European Union's Seventh Framework Program FP/2013–2018/ERC Grant 336077.

1. H. A. Lowenstam, S. Weiner, *On Biomineralization* (Oxford University Press, 1989).
2. S. Raz, S. Weiner, L. Addadi, Formation of high-magnesian calcites via an amorphous precursor phase: Possible biological implications. *Adv. Mater.* **12**, 38–42 (2000).
3. C. Moureaux *et al.*, Structure, composition and mechanical relations to function in sea urchin spine. *J. Struct. Biol.* **170**, 41–49 (2010).
4. S. Bentov, J. Erez, Impact of biomineralization processes on the Mg content of foraminiferal shells: A biological perspective. *Geochem. Geophys. Geosyst.* **7**, Q01P08 (2006).
5. L. E. Wasylenki, P. M. Dove, J. J. De Yoreo, Effects of temperature and transport conditions on calcite growth in the presence of Mg2+: Implications for paleothermometry. *Geochim. Cosmochim. Acta* **69**, 4227–4236 (2005).
6. X. Long, Y. Ma, L. Qi, Biogenic and synthetic high magnesium calcite: A review. *J. Struct. Biol.* **185**, 1–14 (2014).
7. Y. Ma, S. R. Cohen, L. Addadi, S. Weiner, Sea urchin tooth design: An "all-calcite" polycrystalline reinforced fiber composite for grinding rocks. *Adv. Mater.* **20**, 1555–1559 (2008).
8. Y. Ma *et al.*, The grinding tip of the sea urchin tooth exhibits exquisite control over calcite crystal orientation and Mg distribution. *Proc. Natl. Acad. Sci. U.S.A.* **106**, 6048–6053 (2009).
9. I. Polishchuk *et al.*, Coherently aligned nanoparticles within a biogenic single crystal: A biological prestressing strategy. *Science* **358**, 1294–1298 (2017).
10. R. Z. Wang, L. Addadi, S. Weiner, Design strategies of sea urchin teeth: Structure, composition and micromechanical relations to function. *Philos. Trans. R. Soc. Lond. B Biol. Sci.* **352**, 469–480 (1997).
11. S. Gayathri *et al.*, In vitro study of magnesium-calcite biomineralization in the skeletal materials of the seastar *Pisaster giganteus*. *Chemistry* **13**, 3262–3268 (2007).
12. I. Sethmann, G. Wörheide, Structure and composition of calcareous sponge spicules: A review and comparison to structurally related biominerals. *Micron* **39**, 209–228 (2008).
13. D. Vielzeuf *et al.*, Distribution of sulphur and magnesium in the red coral. *Chem. Geol.* **355**, 13–27 (2013).
14. D. W. J. Bosence, "Coralline algae: Mineralization, taxonomy, and palaeoecology" in *Calcareous Algae and Stromatolites*, R. Riding, Ed. (Springer, 1991), pp. 98–113.
15. N. A. Kamenos, M. Cusack, T. Huthwelker, P. Lagarde, R. E. Scheibling, Mg-lattice associations in red coralline algae. *Geochim. Cosmochim. Acta* **73**, 1901–1907 (2009).
16. K. J. Davis, P. M. Dove, J. J. De Yoreo, The role of Mg2+ as an impurity in calcite growth. *Science* **290**, 1134–1137 (2000).

17. G. Falini, S. Fermani, M. Gazzano, A. Ripamonti, Structure and morphology of synthetic magnesium calcite. *J. Mater. Chem.* **8**, 1061–1065 (1998).
18. G. Magnabosco *et al.*, Non-stoichiometric hydrated magnesium-doped calcium carbonate precipitation in ethanol. *Chem. Commun. (Camb.)* **55**, 12944–12947 (2019).
19. E. Loste, R. M. Wilson, R. Seshadri, F. C. Meldrum, The role of magnesium in stabilising amorphous calcium carbonate and controlling calcite morphologies. *J. Cryst. Growth* **254**, 206–218 (2003).
20. L. Addadi, S. Raz, S. Weiner, Taking advantage of disorder: Amorphous calcium carbonate and its roles in biomineralization. *Adv. Mater.* **15**, 959–970 (2003).
21. Y. Politi *et al.*, Role of magnesium ion in the stabilization of biogenic amorphous calcium carbonate: A structure—function investigation. *Chem. Mater.* **22**, 161–166 (2010).
22. L. B. Gower, Biomimetic model systems for investigating the amorphous precursor pathway and its role in biomineralization. *Chem. Rev.* **108**, 4551–4627 (2008).
23. C. R. Blue, P. M. Dove, Chemical controls on the magnesium content of amorphous calcium carbonate. *Geochim. Cosmochim. Acta* **148**, 23–33 (2015).
24. R. D. Shannon, Revised effective ionic radii and systematic studies of interatomic distances in halides and chalcogenides. *Acta Crystallogr. A* **32**, 751–767 (1976).
25. E. Seknazi, B. Pokroy, Residual strain and stress in biocrystals. *Adv. Mater.* **30**, e1707263 (2018).
26. M. E. Kunitake, S. P. Baker, L. A. Estroff, The effect of magnesium substitution on the hardness of synthetic and biogenic calcite. *MRS Commun.* **2**, 113–116 (2012).
27. E. Seknazi *et al.*, From spinodal decomposition to alternating layered structure within single crystals of biogenic magnesium calcite. *Nat. Commun.* **10**, 1–9 (2019).
28. N. Bianco-Stein *et al.*, Structural and chemical variations in Mg-calcite skeletal segments of coralline red algae lead to improved crack resistance. *Acta Biomater.* **130**, 362–373 (2021).
29. G. Hendler, M. Byrne, Fine structure of the dorsal arm plate of *Ophiocoma wendti*: Evidence for a photoreceptor system (Echinodermata, Ophiuroidea). *Zoomorphology* **107**, 261–272 (1987).
30. J. Aizenberg, A. Tkachenko, S. Weiner, L. Addadi, G. Hendler, Calcitic microlenses as part of the photoreceptor system in brittlestars. *Nature* **412**, 819–822 (2001).
31. H. W. Johansen, *Coralline Algae: A First Synthesis* (CRC Press, 2018).
32. P. T. Martone *et al.*, Mechanics without muscle: Biomechanical inspiration from the plant world. *Integr. Comp. Biol.* **50**, 888–907 (2010).
33. P. T. Martone, L. Kost, M. Boller, Drag reduction in wave-swept macroalgae: Alternative strategies and new predictions. *Am. J. Bot.* **99**, 806–815 (2012).
34. N. Bianco-Stein *et al.*, Helical microstructures of the mineralized coralline red algae determine their mechanical properties. *Adv. Sci. (Weinh.)* **7**, 2000108 (2020).
35. M. A. Borowitzka, A. W. D. Larkum, Calcification in algae: Mechanisms and the role of metabolism. *Crit. Rev. Plant Sci.* **6**, 1–45 (1987).
36. K. E. Chave, Physics and chemistry of biomineralization. *Annu. Rev. Earth Planet. Sci.* **12**, 293–305 (1984).
37. R. Riding, *Calcareous Algae and Stromatolites* (Springer Science & Business Media, 2012).
38. D. Vielzeuf, J. Garrabou, A. Baronnet, O. Grauby, C. Marschal, Nano to macroscale biomineral architecture of red coral (*Corallium rubrum*). *Am. Mineral.* **93**, 1799–1815 (2008).
39. P. Fratzl, R. Weinkamer, Nature's hierarchical materials. *Prog. Mater. Sci.* **52**, 1263–1334 (2007).
40. J. Seto *et al.*, Structure-property relationships of a biological mesocrystal in the adult sea urchin spine. *Proc. Natl. Acad. Sci. U.S.A.* **109**, 3699–3704 (2012).
41. F. Mastropietro *et al.*, Revealing crystalline domains in a mollusc shell single-crystalline prism. *Nat. Mater.* **16**, 946–952 (2017).
42. J. M. Walker, B. Marzec, N. Ozaki, D. Clare, F. Nudelman, Morphological development of Pleurochrysis carterae coccoliths examined by cryo-electron tomography. *J. Struct. Biol.* **210**, 107476 (2020).
43. V. Schoeppler *et al.*, Biomineralization as a paradigm of directional solidification: A physical model for molluscan shell ultrastructural morphogenesis. *Adv. Mater.* **30**, e1803855 (2018).
44. V. Schoeppler *et al.*, Shaping highly regular glass architectures: A lesson from nature. *Sci. Adv.* **3**, eaao2047 (2017).
45. S.-M. Chao, C.-C. Tsai, Reproduction and population dynamics of the fissiparous brittle star *Ophiactis savignyi* (Echinodermata: Ophiuroidea). *Mar. Biol.* **124**, 77–83 (1995).
46. M. E. Kunitake, L. M. Mangano, J. M. Peloquin, S. P. Baker, L. A. Estroff, Evaluation of strengthening mechanisms in calcite single crystals from mollusk shells. *Acta Biomater.* **9**, 5353–5359 (2013).
47. R. C. Pond, F. R. N. Nabarro, *Dislocations in Solids* (North Holland, Amsterdam, the Netherlands, 1989).
48. U. F. Kocks, A. S. Argon, M. F. Ashby, Models for macroscopic slip. *Prog. Mater. Sci.* **19**, 171–229 (1975).
49. J. Ihli *et al.*, Strain-relief by single dislocation loops in calcite crystals grown on self-assembled monolayers. *Nat. Commun.* **7**, 11878 (2016).
50. E. Orowan, Symposium on internal stresses in metals and alloys. *Nature* **164**, 296 (1949).
51. A. J. E. Foreman, M. J. Makin, Dislocation movement through random arrays of obstacles. *Can. J. Phys.* **45**, 511–517 (1967).
52. K. Hanson, J. W. Morris Jr., Estimation of the critical resolved shear stress for dislocation glide through a random mixture of distinct obstacles. *J. Appl. Phys.* **46**, 2378–2383 (1975).
53. A. G. Evans, T. Langdon, Structural ceramics. *Prog. Mater. Sci.* **21**, 171–425 (1976).
54. Y. Politi, T. Arad, E. Klein, S. Weiner, L. Addadi, Sea urchin spine calcite forms via a transient amorphous calcium carbonate phase. *Science* **306**, 1161–1164 (2004).
55. E. Loste, F. C. Meldrum, Control of calcium carbonate morphology by transformation of an amorphous precursor in a constrained volume. *Chem. Commun. (Camb.)* **2001**, 901–902 (2001).
56. E. Beniash, J. Aizenberg, L. Addadi, S. Weiner, Amorphous calcium carbonate transforms into calcite during sea urchin larval spicule growth. *Proc. R. Soc. London. Ser. B Biol. Sci.* **264**, 461–465 (1997).
57. C. S. Haase, J. Chadam, D. Feinn, P. Ortoleva, Oscillatory zoning in plagioclase feldspar. *Science* **209** 272–274 (1980).
58. C. J. Allegre, A. Provost, C. Jaupart, Oscillatory zoning: A pathological case of crystal growth. *Nature* **294**, 223–228 (1981).
59. P. Fratzl, O. Penrose, J. L. Lebowitz, Modeling of phase separation in alloys with coherent elastic misfit. *J. Stat. Phys.* **95**, 1429–1503 (1999).